

Investigating Lithium Segregation in Nickel-Rich Layered Oxides via Atom Probe Tomography and its Impact on Performance

Peddi Mahender Reddy^{+, [a]}, Sasikala Natarajan^{+, [a]}, Nagini Macha,^[b] Raghavan Gopalan,^[a] and Sahana B Moodakare^{*[a]}

Nickel-rich $\text{LiNi}_{0.8}\text{Co}_{0.15}\text{Al}_{0.05}\text{O}_2$ (NCA) is a promising alternative to $\text{LiNi}_{1-x-y}\text{Co}_x\text{Mn}_y\text{O}_2$ (NMC) with $x + y \leq 0.2$, providing high specific energy and power density, making it ideal for long-range electric vehicles. However, the formation of surface residual impurities and extreme sensitivity to moisture are detrimental to the large-scale synthesis and electrochemical performance of NCA. This paper investigates the formation of Li_2CO_3 surface impurities and the elemental distribution of lithium within the secondary particle in NCA synthesized with different lithium-to-transition metal ratios. X-ray diffraction (XRD), Fourier transform infrared spectroscopy (FTIR), and Raman spectroscopy confirm the presence of Li_2CO_3 on the

surface of NCA prepared with 3% excess lithium. Atom probe tomography (APT) analysis of the particle interior confirms the absence of carbonaceous products within the hierarchical structure. Instead, it reveals the segregation of lithium ions into discrete regions, which leads to the poor electrochemical performance of NCA synthesized with excess Li. Upon storage, the structural and electrochemical deterioration is more pronounced in NCA with a 3% excess of lithium than the one prepared without excess lithium, as confirmed by XRD, Raman imaging, and electrochemical galvanostatic charge-discharge testing.

1. Introduction

Recent advancements in lithium-based batteries and their chemistries have had a significant technological impact, particularly in the portable electronics, automotive, and sustainable energy sectors. The demand for increased energy density and cycle life has driven both industry and academia to develop high-energy storage materials that are cost-effective and safe. Ternary layered oxide cathodes, with alternating layers of lithium and transition metal ions, have become one of the most important positive electrode materials for lithium-ion batteries due to their high specific capacity, improved energy efficiency, and cost-effectiveness. Ni-rich $\text{LiNi}_{1-x-y}\text{Co}_x(\text{Mn}/\text{Al})_y\text{O}_2$ (NMC/NCA) can deliver a specific discharge capacity of $\geq 210 \text{ mAhg}^{-1}$ with long-term cyclability and high rate capability. However, these cathode materials still suffer structural, thermal, and mechanical degradation during the long-term cycling/aging of NMC/NCA cells. To achieve a stoichiometric NMC/NCA, stringent synthesis conditions such as using precursors without secon-

dary phases, an optimum calcination temperature, and controlled oxygen flow are required to avoid forming residual impurities.^[1,2]

Although layered oxide cathodes can be synthesized using various techniques, the most conventional method involves the co-precipitation of transition metal (TM) salts (e.g., sulfates, nitrates, or acetates of Ni, Co, Mn/Al) as hydroxides or carbonates, followed by high-temperature heat treatment with lithium salts to form Li-TM oxides.^[3] A slight excess of lithium salt is typically added to compensate for lithium loss during high-temperature calcination caused by its high volatility and to achieve stoichiometric NMC/NCA layered oxides with reduced cation mixing. The Li-to-TM precursor ratio is usually maintained between 1.02 and 1.05.^[4] Unfortunately, unreacted lithium on the surface, existing as Li_2O , interacts with atmospheric moisture and gases to form Li_2CO_3 and LiOH surface impurities, as shown in the following reactions (equation 1–3).^[4]



washing the precursor and final oxide with water is beneficial for removing anionic residues from transition metal salts and impurities formed during the calcination process. However, this washing process induces surface structural changes, such as cationic disorder and the formation of the NiO rock-salt phase. Ni ion in the 3+ oxidation state is susceptible to the Jahn-Teller effect, leading to lattice distortions. These distortions promote

[a] P. M. Reddy,⁺ S. Natarajan,⁺ R. Gopalan, S. B. Moodakare

Centre for Automotive Energy Materials, International Advanced Research Centre for Powder Metallurgy and New Materials, Taramani, Chennai – 600113, India

E-mail: sahanamb@arci.res.in

[b] N. Macha

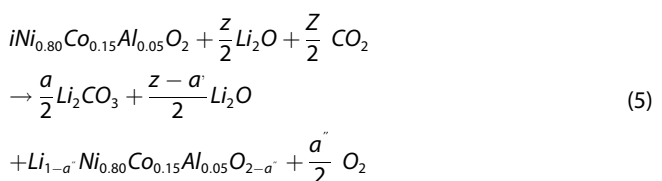
Centre for Nanomaterials (CNM) International Advanced Research Centre for Powder Metallurgy and New Materials, Balapur Post, Hyderabad – 500005, India

⁺ equal contribution

Supporting information for this article is available on the WWW under <https://doi.org/10.1002/batt.202400752>

the reduction of Ni^{3+} to the more stable Ni^{2+} state, resulting in the formation of the NiO phase with the simultaneous release of oxygen ions. These active oxygen ions readily react with the environment, leading to the generation of residual impurities.

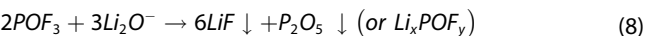
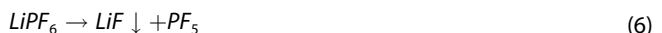
Additionally, the thickness of this impurity layer increases during storage or transport when exposed to air and CO_2 . To mitigate the adverse effects of water washing, non-aqueous solvents containing hydroxyl groups have been suggested as alternatives. While both NMC and NCA layered oxide cathodes are highly reactive with atmospheric moisture and CO_2 , research by Kenji Shizuka et al. indicates that $\text{Li}_{1+x}\text{Ni}_{0.8}\text{Co}_{0.15}\text{Al}_{0.05}\text{O}_2$ (NCA) exhibits greater reactivity due to the higher instability of Ni^{3+} ions and the dissolution of Al^{3+} during washing.^[5] Interaction with CO_2 initially consumes lithium from the surface, and with prolonged exposure, it extracts lithium directly from the NCA lattice, as illustrated in equations (4) and (5).^[6,7]



where $a' + a'' = a$, $0 \leq a' \leq z$, $0 \leq a'' \leq 1$.

Along with causing unwanted structural changes in NCA, lithium residue presents challenges in the electrode slurry formulation. Cathode slurry formulations typically consist of NMC/NCA cathode active materials, conductive carbon, and polyvinylidene fluoride (PVDF) as a binder dissolved in N-methyl-2-pyrrolidone (NMP) solvent. The presence of highly alkaline $\text{LiOH}/\text{Li}_2\text{CO}_3$ salts with a $\text{pH} > 11$ on the surface of the layered oxide cathode material induces dehydrofluorination of PVDF through nucleophilic reactions. This results in crosslinked conjugated polyenes forming, leading to slurry gelation, which hinders uniform electrode coating. Consequently, these Ni-rich layered oxide cathodes are always stored in tightly vacuum-sealed containers to prevent interaction with surface moisture and atmospheric CO_2 .^[8,9]

The formed $\text{LiOH}/\text{Li}_2\text{CO}_3$ layer on the surface of the cathode material is non-conductive, inhibiting the diffusion of Li^+ at the cathode-electrolyte interface and leading to irreversible capacity loss, which in turn reduces the coulombic efficiency. Moreover, OH^- ions from LiOH react to form H_2O molecules, which further react with the electrolyte salt LiPF_6 (as shown in equations 6–8 below). This reaction results in the formation of a LiF layer that impedes lithium-ion movement and causes electrochemical degradation, along with HF gas, which can trigger thermal runaway.



Jung et al. reported the surface reactivity of NMC811 and NMC111 using Raman and X-ray photoelectron spectroscopy (XPS) and estimated the percentage of carbonate contents via gas chromatography.^[10] $\text{LiNi}_{0.8}\text{Co}_{0.1}\text{Mn}_{0.1}\text{O}_2$ was exposed to H_2O and CO_2 for 28 days. The formation of lithium-rich residual impurities was confirmed at intergranular cracks and within the porosity between secondary particles. This was achieved by analyzing changes in the surface elemental distribution using secondary ion mass spectroscopy (SIMS) and scanning electron microscopy (SEM).^[11]

Although several research papers focus on the addition of excess Li during synthesis, leading to the formation of residual impurities on the surface and affecting the storage characteristics of Ni-rich layered oxide cathodes, the corresponding impact within the secondary oxide particles has not been investigated in detail. Understanding the lithium residues inside the nano hierarchical architecture is equally important, as it decomposes to O_2 and produces superoxide in a lithium-ion cell when charged. Superoxide attacks the electrolyte, leading to the formation of Li_2CO_3 accumulation. Li_2CO_3 decomposes to CO_2 at approximately 3.82 V vs. Li/Li^+ , releasing CO_2 . While this may increase only polarization in coin cells, it poses safety hazards in larger cells, necessitating a detailed investigation to understand what happens within the nano-micro-hierarchical structure of nickel-rich layered oxides when excess lithium precursors relative to the transition metals are used.^[9,12]

This manuscript investigates the influence of excess lithium addition on the elemental distribution within spherical aggregates using atom probe tomography. $\text{LiNi}_{0.8}\text{Co}_{0.15}\text{Co}_{0.15}\text{Al}_{0.05}\text{O}_2$ was synthesized with two different $\text{Ni}_{0.8}\text{Co}_{0.15}\text{Al}_{0.05}(\text{OH})_2/\text{Li}$ ratios, 1:1 and 1:03, to determine the extent of lithium residual impurity formation across the nano-micro hierarchical structure. X-ray diffraction (XRD), Fourier Transform Infrared Spectroscopy (FTIR) and Raman analyses confirm the formation of a thin layer of Li_2CO_3 on the surface of the oxide particles. The influence of the Li:TM ratio on the electrochemical performance of NCA was investigated using galvanostatic charge-discharge cycling and rate performance testing at various C-rates within a voltage window of 2.8–4.2 V vs. Li/Li^+ . Furthermore, the physicochemical stability of the oxide material aged for almost 1 year was examined using XRD, FTIR, Raman mapping, and electrochemical analysis to understand the material's shelf life with different lithium-to-TM ratios.

Experimental

Material Preparation

$\text{LiNi}_{0.8}\text{Co}_{0.15}\text{Al}_{0.05}\text{O}_2$ (NCA) was synthesized through a solid-state reaction of NCA hydroxide ($\text{Ni}_{0.8}\text{Co}_{0.15}\text{Al}_{0.05}(\text{OH})_2$) and lithium hydroxide ($\text{LiOH}\cdot\text{H}_2\text{O}$). The NCA hydroxide was prepared using the co-precipitation method in a batch reactor. A stoichiometric mixture of a 2 M solution of NiSO_4 , CoSO_4 , and $\text{Al}_2(\text{SO}_4)_3$ was pumped into the reactor at a 2 ml/min rate using a syringe pump.

The pH of the solution in the reactor was maintained at 11 by adding a 4 M NaOH solution at the same rate via a syringe pump. A 4 M NH₃OH solution was separately pumped into the reactor using a peristaltic pump at 2 ml/min. The resulting hydroxide precipitate was washed with deionized water to remove sulfate ions. The washed hydroxide powder was dried at 120 °C under vacuum to remove moisture. The NCA hydroxide powder was mixed and calcined with LiOH in two ratios. In the first sample, the stoichiometric ratio of NCA hydroxide to LiOH was 1:1, named Li:NCA-1:1. In the second sample, a 3 wt% excess LiOH was used, resulting in a Li:NCA-1.03:1 ratio. The mixed hydroxide sample was subjected to a two-stage calcination process: first at 450 °C for 5 hours and then at 850 °C for 15 hours in an oxygen atmosphere.

Structural and Electrochemical Characterization

Powder X-ray diffraction (XRD) measurements were performed using a Rigaku diffractometer with Cu K-alpha radiation. The Fourier-transform infrared (FTIR) spectra of the samples were recorded using a Bruker VERTEX 70v vacuum spectrometer in ATR/FTIR mode with 32 scans and a resolution of 2 cm⁻¹. The Raman spectra were recorded using a WiTec Alpha 300 system with a 532 nm laser beam. The morphology of the oxide powders was analyzed using scanning electron microscopy (SEM, Quanta 400-FEG) equipped with a field emission gun operating at 30 kV. Elemental distribution in both samples was analyzed using atom probe tomography (APT, LEAP 5000 XR).

Electrode laminates were prepared by coating a slurry consisting of 80 wt% Li:NCA-1:1/Li:NCA-1.03:1, 15 wt% carbon black, and 5 wt% PVDF binder in N-methyl-2-pyrrolidone (NMP) onto an aluminum current collector using a doctor blade. After coating, the electrodes were dried overnight in a vacuum oven at 120 °C to remove residual solvent. Electrochemical testing was performed using a 2032-coin cell configuration. A glass fiber separator and an electro-

lyte comprising 1 M LiPF₆ dissolved in an organic solvent mixture of equal proportions of ethylene carbonate (EC), ethyl methyl carbonate (EMC), and dimethyl carbonate (DMC) were used.

2. Results and Discussion

2.1 Structural Properties of p-Li:NCA-1:1 and p-Li:NCA-1.03:1

The electrochemical performance of nickel-rich layered oxides is significantly influenced by their chemical composition, microstructure, stoichiometry, secondary phases, and the percentage of Li⁺/Ni²⁺ antisite defect. The effect of the stoichiometric ratio of Li:NCA on the structural properties of NCA was investigated using XRD, FTIR, Raman, and APT. Figure 1a displays the X-ray diffraction patterns of p-Li:NCA-1:1 and p-Li:NCA-1.03:1, showing typical reflections characteristic of NCA layered oxides. The XRD patterns are indexed based on the standard powder diffraction pattern of layered oxides (ICDD 98-007-9167).^[13] The observed XRD pattern confirms the formation of rhombohedral-structured stoichiometric NCA with $R\bar{3}c$ space group. Though both samples crystallized in rhombohedral crystal structures, closer insight into the XRD pattern revealed a few notable observations in the high Li content NCA (p-Li:NCA-1.03:1). The enlarged view of XRD in the 20 = 20–35° region is given in Figure 1b. The standard XRD pattern of Li₂CO₃ is also provided in Figure 1b. In the XRD pattern of p-Li:NCA-1.03:1, additional peaks closely match the Li₂CO₃ standard pattern (ICDD 01-087-0729). The high-intensity peaks of Li₂CO₃ at 20 = 31.7°, 21.34° and 31.64° are present in p-Li:NCA-1.03:1 and are absent in p-

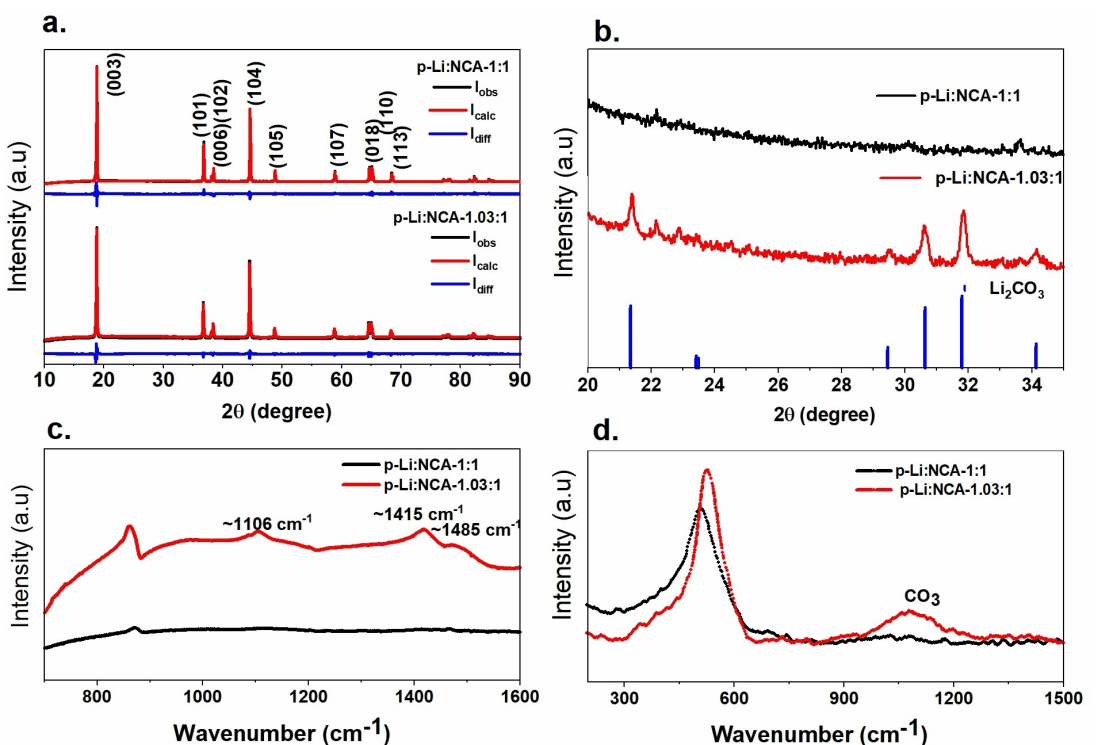


Figure 1. (a) X-ray diffraction studies of p-Li:NCA-1:1 and p-Li:NCA-1.03:1, (b) Magnified XRD in the 20 = 20–35° region along with standard pattern of Li₂CO₃, (c) FTIR, and (d) Raman spectra of p-Li:NCA-1:1 and p-Li:NCA-1.03:1.

Li:NCA-1:1. To quantify the percentage of Li_2CO_3 and NCA, the XRD pattern is refined with two phases, NCA and Li_2CO_3 . The percentage of Li_2CO_3 in p-Li:NCA-1.03:1 is 3.7% and refinement of p-Li:NCA-1:1 confirmed the negligible presence of Li_2CO_3 . The fit parameters are given in Table 1.

The electrochemical performance of layered oxides depends on the level of hexagonal ordering and the degree of $\text{Li}^+/\text{Ni}^{2+}$ cation mixing. Low cationic mixing and minimal structural degradation indicate favorable conditions for the intercalation and deintercalation of Li ions during cycling. Due to the stability of Ni in the +2 oxidation state, a small concentration of Ni^{2+} is typically present in nickel-rich cathode materials like NCA. Moreover, Ni^{2+} ions can substitute Li^+ ions due to their similar atomic radii. The degree of Ni^{2+} substitution at Li sites can be deduced from the intensity ratio I_{003}/I_{104} in X-ray diffraction (XRD); for p-Li:NCA-1:1, it is 1.31, and for p-Li:NCA-1.03:1, it is 1.14. The hexagonal ordering in these structures can be assessed using the R-factor (the ratio of the intensity of (006) + (102) to (101) reflections) and the c/a lattice parameter ratio. The observed R-factor of p-Li:NCA-1:1 and p-Li:NCA-1.03:1 is 0.41 and 0.58, respectively. A higher I_{003}/I_{104} and low R-value suggests that the amount of Ni^{2+} occupying the Li^+ site is lower in p-Li:NCA-1:1 compared to p-Li:NCA-1.03:1. Also, c/a of p-Li:NCA-1:1 and p-Li:NCA-1.03:1 is 4.944 and 4.942 respectively.^[2] The slightly higher nickel concentration at the Li site in p-Li:NCA-1.03:1 is attributed to the formation of Li_2O due to extra lithium. It is known that the enthalpy of formation is more negative for Li_2O compared to NCA. Therefore, for a given oxygen partial pressure, the conditions may favor the formation of Li_2O , leading to higher defect concentrations in the structure. Although there are separate studies on the enthalpy of the formation of nickel-rich layered oxides and Li_2O , this highlights the need for detailed studies on the enthalpy of formation of defects in NCA and the formation of Li_2O as a function of excess lithium concentration.^[14,15]

The trace amount of Li_2CO_3 in NCA can be analyzed using FTIR and Raman spectroscopy, and the spectra are given in Figures 1c and 1d. The active vibration modes of lithium layered oxides are $\Gamma = \text{A}_{1g} + \text{E}_g + 2\text{A}_u + 2\text{E}_u$, out of which the first two terms are Raman active, and the last two are IR active. A_{1g} and E_g correspond to the vibrations of oxygen atoms, with A_{1g} representing vibrations parallel to the c-axis and E_g representing vibrations perpendicular to the c-axis of LiMO_2 ($\text{M} = \text{Co, Ni, Al}$), respectively. In LiCoO_2 , two distinctive Raman bands, E_g and A_{1g} , are observed at 487 cm^{-1} and 597 cm^{-1} , respectively. In contrast, for LiNiO_2 , the peak position of A_{1g} shifts to 544 cm^{-1} . In $\text{LiNi}_{0.8}\text{Co}_{0.15}\text{Al}_{0.05}\text{O}_2$, these two peaks overlap, resulting in a broad peak observed in the range of 350 to 600 cm^{-1} .

Table 1. Rietveld Refined data of NCA samples lattice constant, a/c and $\text{Li}^+, \text{Ni}^{2+}$.

Sample	a (Å)	C (Å)	c/a	Li^+	Ni^{2+}	R_{wp}
p-Li:NCA-1:1	2.865	14.167	4.944	0.963	0.037	2.38
p-Li:NCA-1.03:1	2.869	14.184	4.942	0.941	0.059	1.87

Accordingly, Raman spectra of both p-Li:NCA-1:1 and p-Li:NCA-1.03:1 consist of a broad peak in the wavenumber range of 350 cm^{-1} to 600 cm^{-1} . The FTIR spectra have five peaks corresponding to 4 internal and one external mode. The low-frequency peak at $\sim 190\text{ cm}^{-1}$ may arise from the external lattice vibration, though the exact peak assignment is difficult.^[15-17] The internal bands correspond to O–M–O stretching and bending of MO_6 and LiO_6 . Raman spectra and FTIR of p-Li:NCA-1.03:1 have peaks corresponding to Li_2CO_3 , which is negligible in the case of p-Li:NCA-1:1. The Li_2CO_3 peak in Raman spectra is observed at 1083 cm^{-1} and in FTIR it is at 1415 cm^{-1} and 1480 cm^{-1} which corresponds to CO_3 symmetric stretching in Li_2CO_3 (Figure 1c and d). An excess amount of LiOH is added to compensate for Li losses at high temperatures^[4,9] during the solid-state synthesis of lithium-layered oxides. From XRD, FTIR, and Raman analysis, it can be concluded that the added excess lithium forms a thin oxide layer of Li_2CO_3 in p-Li:NCA-1.03:1 and is negligible in p-Li:NCA-1:1 at the surface of the particle.

However, these characterization techniques do not give a clear picture of the composition of lithium residuals at the interior of the nano-micro hierarchical aggregates. Hence, atom probe tomography (APT) of a section of material taken from the interior of the aggregate is carried out. Figure S1 shows the single secondary particle SEM micrograph of p-Li:NCA-1:1 and p-Li:NCA-1.03:1. Both samples consist of a nano-micro hierarchical structure, typical of lithium layered oxide prepared by co-precipitation-assisted solid-state synthesis. However, the aggregate size ranged from $6\text{ }\mu\text{m}$ to $15\text{ }\mu\text{m}$. An aggregate of around $10\text{ }\mu\text{m}$ is identified for the APT analysis (Figure 2a). The exterior of the aggregate is milled using FIB (Figure 2b), and a small cantilever of the sample from the center of the aggregate is lifted out using a nano manipulator (Figure 2c). As an example, one of the aggregates from p-Li:NCA-1:1, the small cantilever of the sample, and the region of interest (ROI) are shown in Figure 2a-c, and that of p-Li:NCA-1.03:1 is given in Figure S2. Figure 2d shows the overall elemental mapping of p-Li:NCA-1:1 and individual elemental mapping. Figure 3 shows the overall elemental mapping of p-Li:NCA-1.03:1 and the corresponding individual elemental mapping. In the APT mass-to-charge spectra of both the samples, elemental peaks of Ni, Co, Al, O, and Li are observed along with the various molecular species as given in the mass spectrometry of the samples in Figure S3. However, the mass spectrometry contained no peak corresponding to C or its molecular derivative. This suggests that in the interior of the aggregate, there is no carbonaceous by-product, unlike the surface.

While no elemental segregation is observed in p-Li:NCA-1:1, the non-uniform spatial distribution of Li and TM (transition metal, Ni, Co, Al) is observed in p-Li:NCA-1.03:1. To understand the distribution of Li to other elements, a one-dimensional concentration profile was carried out at various places (Figure S4). There are two distinct regions; in some areas, the stoichiometry of Li:TM is close to one, while in other places, it is as high as 20. In the region where Li is high, TM and oxygen are low in concentration and vice versa, which is a striking feature throughout the samples, as can be observed in the 1-D profile in Figure S4. APT was conducted on two additional sets of

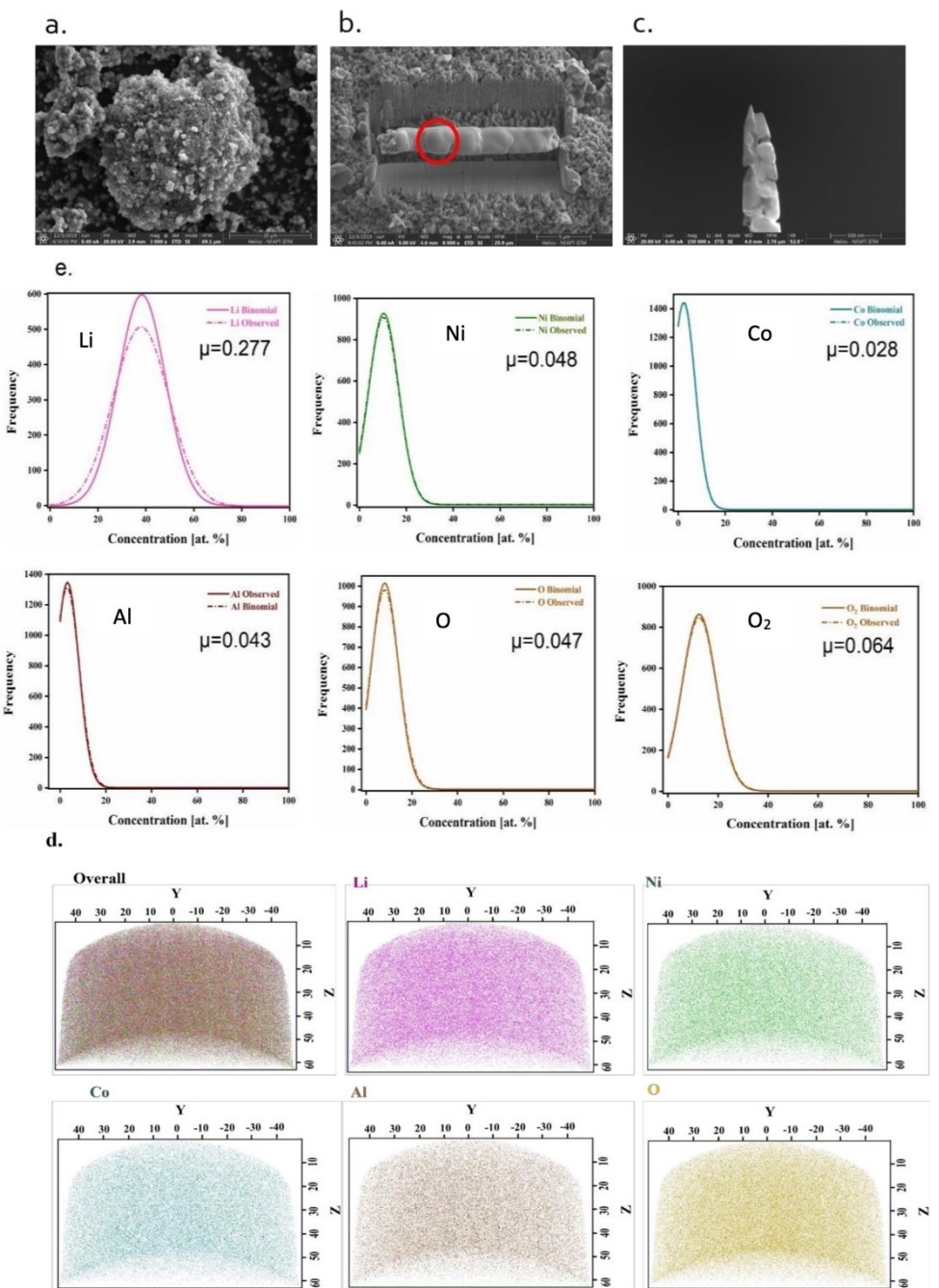


Figure 2. (a) SEM micrograph p-Li:NCA-1:1 (b) selected region for APT analysis (c) cantilever and the region of interest; (d) Atom probe tomography elemental mapping of p-Li:NCA-1:1 (b). Overall elemental mapping and individual elemental mapping is given in respective color (e). frequency distribution of analysis p-Li:NCA-1:1.

samples to confirm the reproducibility of lithium segregation in p-Li:NCA:1.03:1. Similar lithium segregation was observed, and the overall elemental distribution at two different regions of interest (ROI) from p-Li:NCA:1.03:1 is shown in Figure S5b-c.^[18,19]

The segregation of Li in p-Li:NCA-1.03:1 compared to p-Li:NCA-1:1 is further confirmed by the frequency distribution function analysis. A frequency histogram is constructed for the statistical analysis of elemental segregation by dividing the entire APT data into 400 atom bins. Binomial frequency

distribution is expected for a homogenous distribution of the elements. The deviation from this is due to the elemental segregation. The frequency distribution of Li, Ni, Co, Al, and O for p-Li:NCA-1:1 and p-Li:NCA-1.03:1 is given in Figure 2e and Figure 3b, respectively. The higher Pearson coefficient value for Li in p-Li:NCA-1.03:1 confirms the validity of a significant extent of Li segregation at different places. The Pearson coefficient of Li, Ni, Co, Al, and O₂ in p-Li-NCA-1.03:1 is 0.835, 0.31, 0.11, 0.003, and 0.58, and in p-Li:NCA-1:1 it is 0.27, 0.04, 0.02, 0.04, 0.06 respectively. Relatively high values of Pearson

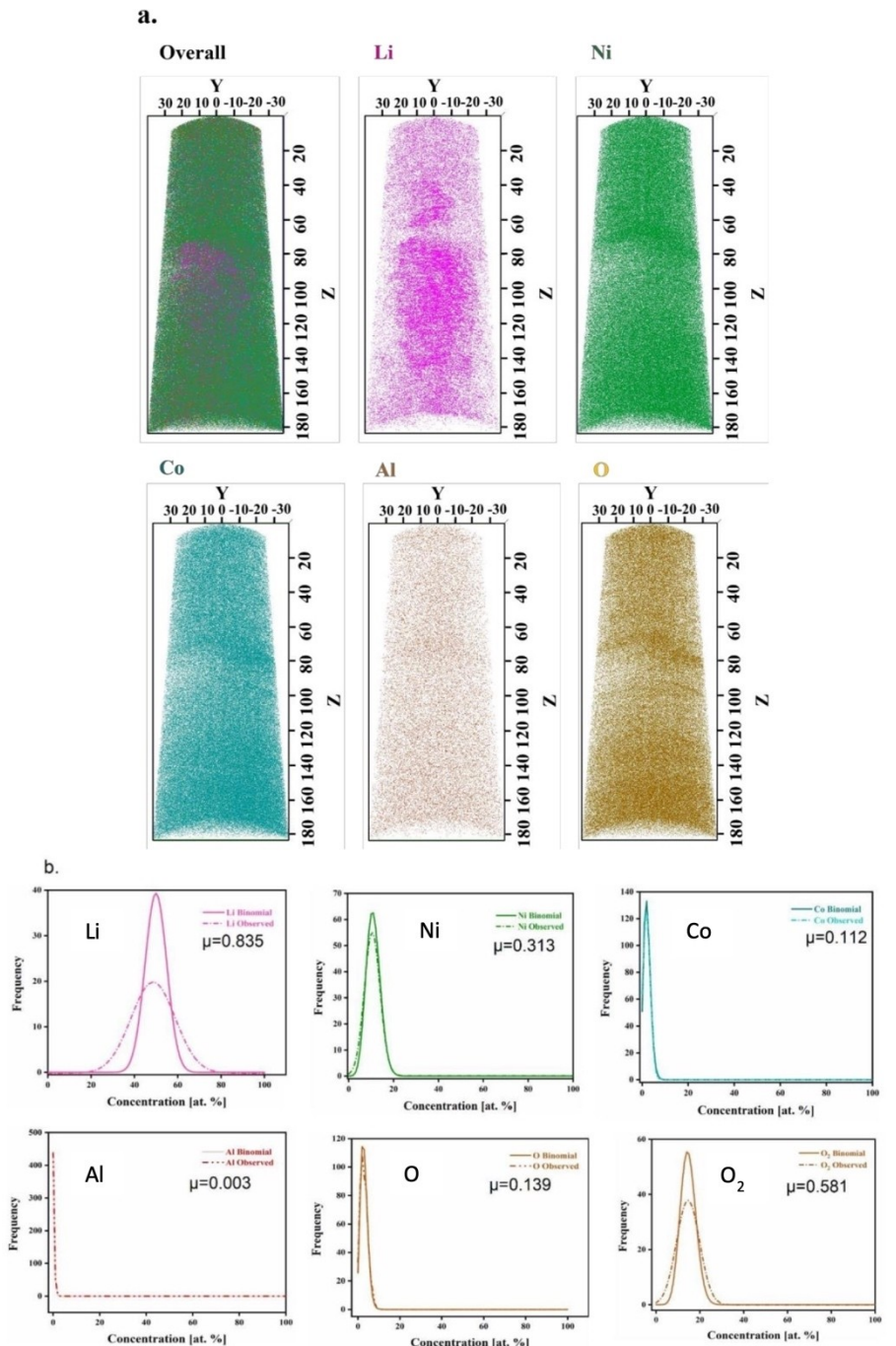


Figure 3. Atom probe tomography elemental mapping of p-Li:NCA-1.03:1 (a) Overall elemental mapping and individual elemental mapping is given in respective color. (b) frequency distribution analysis of the p-Li:NCA-1.03:1 sample.

coefficient of Li in p-Li:NCA-1.03:1 compared to p-Li:NCA-1:1, suggests higher segregation of Li in p-Li:NCA-1.03:1. However, diminutive segregation of Li in p-Li:NCA-1:1 too cannot be ruled out.

2.2. Electrochemical Performance

The presence of electrochemically inactive lithium residuals is known to have several implications on the performance of

batteries. To understand residual lithium's effects on NCA's electrochemical performance, slow charge-discharge tests were conducted at 0.03 C in constant current (CC) mode, followed by GITT measurements. The cells were initially charged and discharged at C/30 in 3–4.2V. A few sets of new cells were fabricated and tested at C/10. The C rate performance was performed at 0.1C, 0.3C, 1C, 3C, and 5C. The cyclic stability testing of cells was carried out at 1C charge and discharge. The profile is shown in Figure 4a-d. There is a significant change in the initial cycling profiles of the samples, with notable

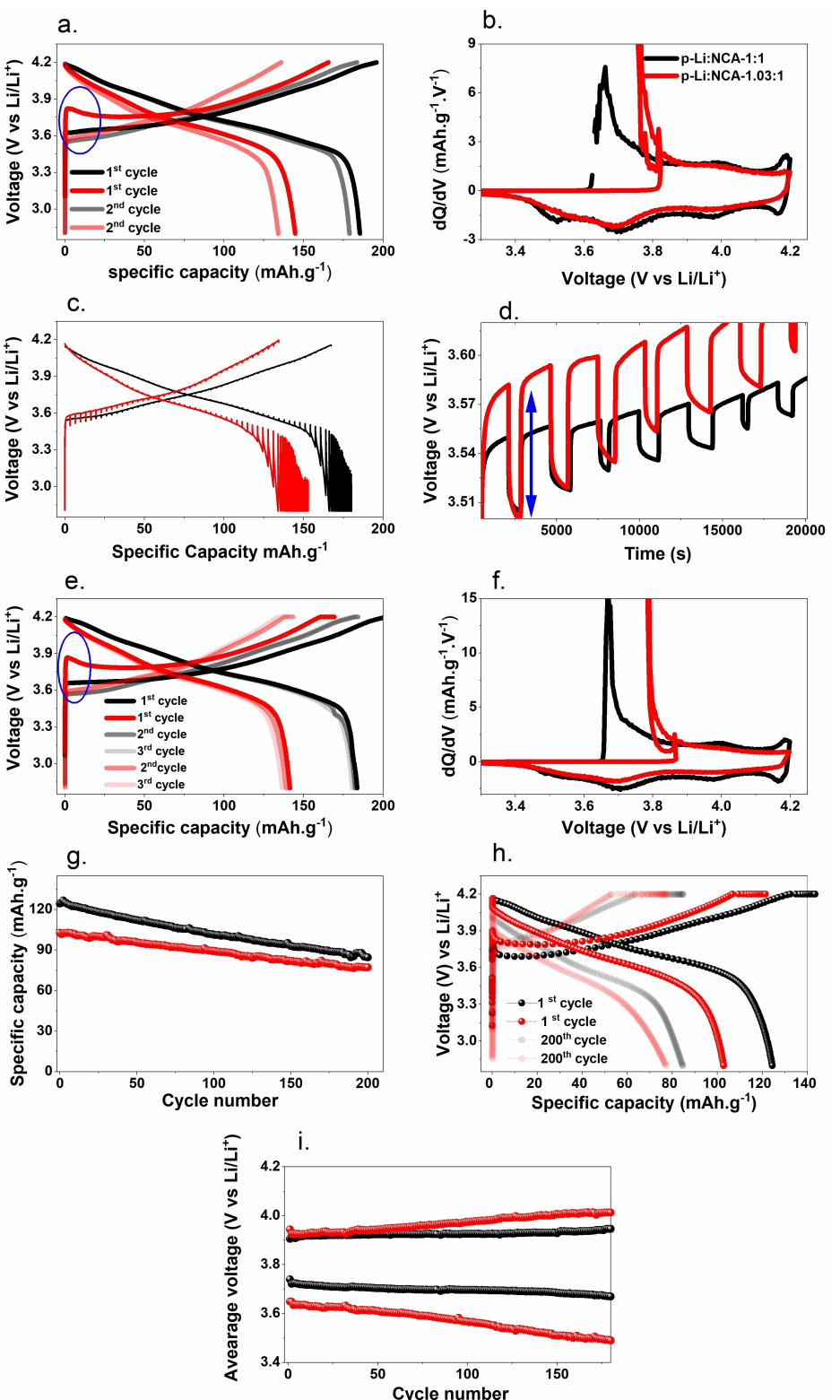


Figure 4. (a) Charge-discharge profiles at 0.03 C, (b) corresponding dQ/dV curves, (c) GITT profiles (d) Magnified GITT profile from 3.5 to 3.65 V, (e) Charge-discharge profiles at 0.1 C, (f) corresponding dQ/dV curves, (g) cyclic stability at 1 C, (h) 1st and 200th cycling charge-discharge curves at 1 C, (i) Average voltage vs. cycle number. Symbol guide: shades of black : p-Li:NCA-1:1, shades of red p-Li:NCA-1.03:1.

irreversibility in the first cycle and a capacity loss from the first to the second cycle, which is more pronounced in p-Li:NCA-1.03:1. Both charge and discharge capacity of p-Li:NCA-1:1 is

higher than p-Li:NCA-1.03:1. The discharge capacity of 185 mAh/g and 145 mAh/g is observed in p-Li:NCA-1:1 and p-Li:NCA-1.03:1 respectively. In addition, the coulombic effi-

ciency of p-Li:NCA-1:1 is 94%, while that of p-Li:NCA-1.03:1 is 87%. In both cells, a reduction in discharge capacity is observed from the first to the second cycle, with a significant decrease in p-Li:NCA-1.03:1, as shown in Table 2. Another set of coin cells was fabricated and subjected to charging under CC-CV mode and discharging in CC mode at 0.1 C, followed by cyclic stability testing at 1 C, as shown in Figure 4e-h. With the increase in the C-rate from 0.03 C to 0.1 C, although the first cycle coulombic efficiency decreased, the discharge capacity remained similar to that at 0.03 C due to CC-CV mode charging. Additionally, the loss in discharge capacity in subsequent cycles was reduced to 2–4 mAh/g. However, the first cycle coulombic efficiency of p-Li:NCA-1.03:1 at 0.1 C and 0.03 C is lower than that of p-Li:NCA-1:1.

In addition, during the first cycle at 0.1 C and 0.03 C charging of p-Li:NCA-1.03:1, an initial voltage jump is observed, in contrast to p-Li:NCA-1:1, as highlighted in Figures 4a and 4e. The first cycle initial voltage jump is higher in p-Li:NCA-1.03:1 compared to p-Li:NCA-1:1, indicating higher polarization. However, the values become similar from the second cycle onwards, as shown in Table 2. The initial voltage peak is attributed to the presence of insulating carbonate layers on the active material particles of p-Li:NCA-1.03:1.^[10] The absence of the voltage peak from the second cycle onward and the higher irreversibility in the first cycle are due to the decomposition of the carbonate impurities during the first cycle. The absence of the initial voltage peak further confirms the negligible presence of Li₂CO₃ in p-Li:NCA-1:1. To understand the effect of decomposed carbonate on polarization, GITT was performed with 30-minute pulses and 3-hour relaxation times after two cycles at 0.03 C, as shown in Figure 4c. At all values of x in Li_{1-x}Ni_{0.8}Co_{0.15}Al_{0.05}O₂, the initial rise in voltage during pulsing and relaxation is higher in p-Li:NCA-1.03:1. This is evident in the magnified GITT profile during a few pulses in Figure 4d. Due to polarization caused by the insulating impurity, the capacity p-Li:NCA-1.03:1 is lower.

Three different phase transitions in Ni-rich cathode materials contribute to the stored capacity. For Li_{1-x}Ni_{0.8}Co_{0.15}Al_{0.05}O₂, when x < 0.55, the transition is from the hexagonal phase H1 to the monoclinic phase M; when 0.55 ≤ x ≤ 0.75, the transition is from M to hexagonal phase H2; and when x > 0.75, the final transition is from hexagonal phase H2 to hexagonal phase H3.^[13] In p-Li:NCA-1:1, lithium extraction occurs up to x ~0.75,

while in p-Li:NCA-1.03:1, it occurs up to x ~0.62 when charged to 4.2 V at 0.1 C. The difference in lithium extraction is due to a change in polarization at the beginning of the cycle. This is evident in the dQ/dV curves of the first cycle shown in Figures 4b and 4f. The differential voltage curves consist of four distinctive peaks. One sharp peak at the beginning represents kinetic hindrance, while the remaining peaks represent the different phase transitions in NCA. The kinetic hindrance peak against the Li-ion diffusion in the sample is observed at a higher voltage in p-Li:NCA-1.03:1 at both 0.1 C and 0.03 C, compared with p-Li:NCA-1:1. The capacity of the cell depends on the amount of lithium extraction from the structure, which is influenced by the upper cutoff voltage. The incremental capacity curve shows three clear phase transitions in p-Li:NCA-1:1. However, the peak intensity is lower in the case of p-Li:NCA-1.03:1. Additionally, the last phase transition, H2-H3, is not fully activated in p-Li:NCA-1.03:1, resulting in the observed lower capacity at both 0.1 C and 0.03 C.

In addition, it is expected that lithium residuals inside the aggregates will affect the stress experienced by nickel-rich layered oxides during charging and discharging. However, in the current study, due to the presence of Li₂CO₃ on the surface and Li₂O-like secondary phases within the structure, the polarization during charging and discharging differs between p-Li:NCA-1.03:1 and p-Li:NCA-1:1. Consequently, even though both are charged to the same cutoff voltage, the transition from the M phase to the hexagonal H2 phase does not occur in the case of p-Li:NCA-1.03:1. Therefore, establishing a direct correlation between stress during charging and discharging would require advanced techniques such as in-situ XRD, which is not currently addressed in this study. The absence or presence of a transition from the M phase to the hexagonal H2 phase will also influence cyclic stability. Consequently, the cells cycled at 0.1 C are tested for cyclic stability at 1 C. Although the discharge capacity of p-Li:NCA-1:1 at 1 C is higher than that of p-Li:NCA-1.03:1, p-Li:NCA-1.03:1 demonstrates better cyclic stability. After 200 cycles at 1 C, the capacity retention of p-Li:NCA-1:1 is 68%, compared to 76% for p-Li:NCA-1.03:1. However, even after 200 cycles, the capacity of p-Li:NCA-1:1 remains higher than that of p-Li:NCA-1.03:1 and it exhibits lower polarization. The reduced polarization of p-Li:NCA-1:1 throughout the cycles is evident in the average voltage vs. cycle number curves shown in Figure 4i. The charge-discharge

Table 2. Coulombic efficiency and discharge capacity of p-Li:NCA-1:1 and p-Li:NCA-1.03:1 of two sets of coin cells charged-discharged at (i) 0.03 under CC mode and (ii) 0.1 C CC-CV mode.

Sample	0.03 C				0.1 C		
	Cycle number	CE	Discharge capacity (mAh/g)	Initial voltage jump(V vs Li/Li ⁺)	coulombic efficiency	Discharge capacity (mAh/g)	Initial voltage jump(V vs Li/Li ⁺)
p-Li:NCA-1:1	1 st	94	185	3.62	90	184	3.66
	2 nd	97	179	3.54	99	182	3.57
	3 rd	–	–	–	99	181	3.57
p-Li:NCA-1.03:1	1 st	87	145	3.83	83	141	3.87
	2 nd	97	134	3.56	97	139	3.59
	3 rd	–	–	–	98	137	3.59

average voltage of p-Li:NCA-1:1 remains nearly constant, whereas for p-Li:NCA-1.03:1, the average charge voltage increases from 3.92 V to 4 V, and the average discharge voltage decreases from 3.64 V to 3.49 V after 200 cycles. The higher capacity retention of p-Li:NCA-1.03:1 and the significant decrease in average voltage drop may be attributed to the presence of Li_2O within the nano-micro hierarchical structure. As Li_2O can act as a sacrificial salt, it likely helps to retain capacity over prolonged cycling.

To understand the mechanism behind the high overall capacity loss in p-Li:NCA-1:1 and higher average voltage variation p-Li:NCA-1.03:1, dQ/dV of 1st and 200th cycles are analyzed and given in Figure S6a and b. In p-Li:NCA-1.03:1, two peaks are observed in the incremental capacity curve of the first charging cycle, where the first peak consists of the kinetic hindrance and first phase transition, whereas four distinct peaks are observed in p-Li:NCA-1:1. In the 200th cycle, the charging curve has only one peak in p-Li:NCA-1.03:1, corresponding to only the first transition. In contrast, p-Li:NCA-1:1, shows three peaks corresponding to kinetic hindrance and the first two transitions. In the discharge dQ/dV curves of p-Li:NCA-1.03:1, only two peaks corresponding to H2 to M and M to H1 are observed, while in p-Li:NCA-1:1, all three peaks corresponding to different transitions are observed both in the first and 200th cycle. The voltage shift corresponding to H2 to M and M1 to H1 is high in p-Li:NCA-1.03:1; however, the intensity reduction is similar in both samples. This suggests that the irreversibility in the 1st two transitions is identical in the two samples; however, polarization development is more in p-Li:NCA-1.03:1. In p-Li:NCA-1:1, the reduction in the capacity from the third phase transition will also contribute to the

overall capacity loss. The higher polarization development in p-Li:NCA-1.03:1 is due to the byproducts of Li_2CO_3 decomposition from the first cycle carried out at 0.1 C. In p-Li:NCA-1:1, the cycling is further carried out to investigate the effect of the last phase transition on cyclic stability. The capacity retention from 200 to 500 cycles is 80% higher than the initial 200 cycles. This is due to the absence of a third phase transition after 200 cycles, evident in the dQ/dV curves of 350, 400, and 480 cycles (Figure S6c and d).

The C-rate performance of two samples is performed to understand the reversibility of different phase transitions at variable current rates. It is given in Figure 5, along with corresponding incremental capacity curves. The capacity of both cells decreases with an increase in C-rate. The observed specific capacity of p-Li:NCA-1:1 is 178 mAh/g, and p-Li:NCA-1.03:1 is 132 mAh/g at 0.1 C. At 0.3 C, p-Li:NCA-1:1 shows 159 mAh/g and p-Li:NCA-1.03:1 shows 120 mAh/g. The differential capacity curve at 0.3 C is shown in Figure 5b. The H2-H3 phase transition is suppressed in p-Li:NCA-1.03:1, which results in a lower specific capacity. This trend is continued at 1 C, where p-Li:NCA-1.03:1 shows lower capacity than p-Li:NCA-1:1. At 2 C, 3 C, and 5 C, the H2-H3 phase transition is not observed in p-Li:NCA-1:1. At all C rates, the M–H1 transition is observed at lower voltage in p-Li:NCA-1.03:1 compared to p-Li:NCA-1:1 due to higher polarization. Dae-Hyun Cho et al.^[9] demonstrated that the presence of Li_2O leads to the formation of Li_2CO_3 , LiOH , and LiF , as evidenced by X-ray photoelectron spectroscopy and time-of-flight secondary ion mass spectrometry. The lithium residues interact with hydrocarbons generated from the decomposition of the electrolyte, both during contact with the cathode and during charge-discharge cycling. This interaction

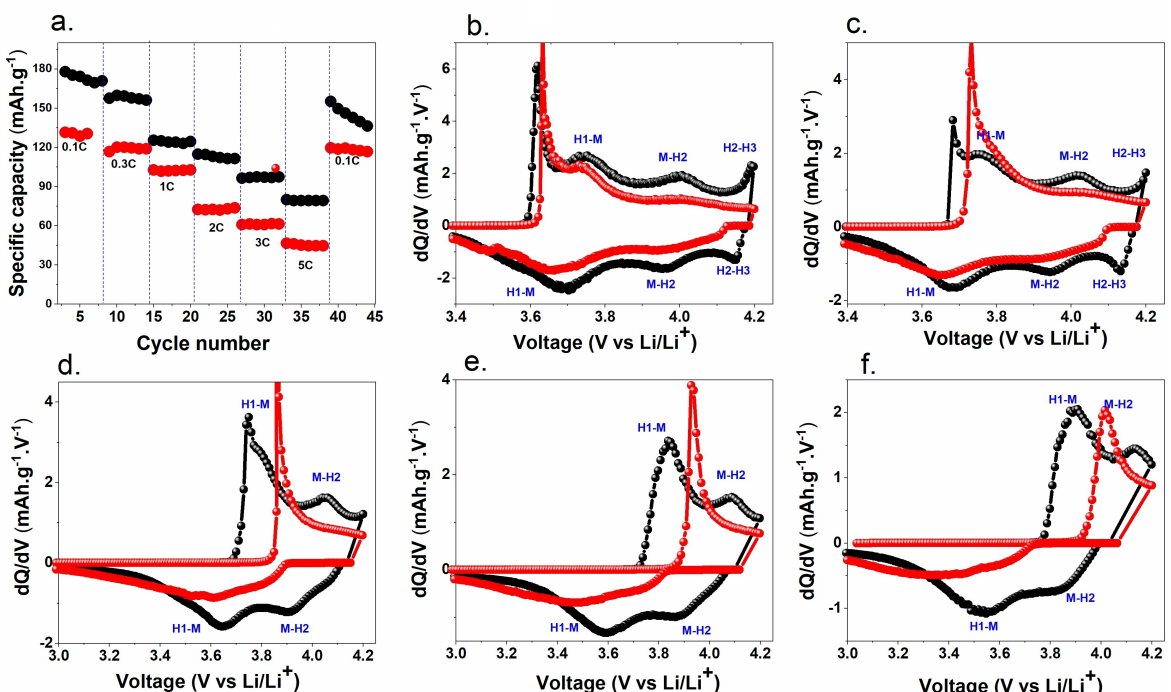


Figure 5. (a) Discharged capacity vs cycle number at different C-rates of p-Li:NCA-1:1 and p-Li:NCA-1.03:1 and incremental capacity curves at (b) 0.3 C, (c) 1 C, (d) 2 C, (e) 3 C, and (f) 5 C. Symbol guide: black dots: p-Li:NCA-1:1; red dots: p-Li:NCA-1.03:1.

produces passive layers on the surface of the active material, which exhibit poor ionic conductivity, thereby deteriorating the electrochemical properties and resulting in low capacity at high C-rates.

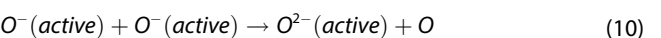
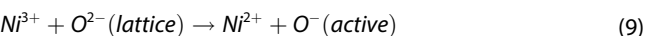
From the various electrochemical analyses of p-Li:NCA-1:1 and p-Li:NCA-1.03:1, it is evident that the presence of Li_2CO_3 increases the polarization; hence, the last phase transition H2 to H3 is not activated in the voltage window of 3 to 4.2 V vs. Li. This leads to lower specific capacity and high polarization development during cycling in p-Li:NCA-1.03:1.^[4]

To understand the effect of material storage (shelf life) on the electrochemical performance, p-Li:NCA-1:1 and p-Li:NCA-1.03:1 are stored in an argon atmosphere for one year and are designated as a-Li:NCA-1.03:1 and a-Li:NCA-1:1. The cells are fabricated using one-year-old active material and are subjected to cycling at 0.1 C for three cycles followed by cycling at 1 C for 200 cycles. The open circuit voltage of a-Li:NCA-1.03:1 and a-Li:NCA-1:1 is close to 1.6 V. Hence, the first charging curve showed an electrolyte decomposition plateau at 2.5 V (Figure 6a). The irreversible capacity in the first cycle of a-Li:NCA-1.03:1 and a-Li:NCA-1:1 are 63 mAh/g and 50 mAh/g, respectively. In both samples, the irreversibility increased with aging. The charge-discharge profile of the second and third cycles of the aged samples, along with the dQ/dV curves, are given in Figures 6b and c. The a-Li:NCA-1:1 exhibited a charge-discharge capacity of 156 mAh/g and 150 mAh/g, while a-Li:NCA-1.03:1 delivered only 124 mAh/g and 120 mAh/g, respectively. The discharged capacity at 0.1 C is reduced by 30 mAh/g in a-Li:NCA-1:1 and 21 mAh/g in a-Li:NCA-1.03:1 after one year of storage. Like pristine samples, the incremental capacity curves of a-Li:NCA-1.03:1 show peaks corresponding to two phase transitions and one kinetic hindrance peak, while a-Li:NCA-1:1 exhibits three-phase transition peaks and one kinetic hindrance peak. The phase transition takes place at a higher voltage in a-Li:NCA-1.03:1 compared to a-Li:NCA-1:1. However, there is no change in the voltage at which various phase transitions occur between the pristine and the aged samples of Li:NCA-1:1 and Li:NCA-1.03:1. The capacity at the first cycle at 1 C of a-Li:NCA-1:1 and a-Li:NCA-1.03:1 are 100 mAh/g, and 71 mAh/g and capacity retention of 54% and 50% are observed after 200 cycles respectively. However, the loss in capacity is more significant at the initial ~50 cycles. The loss in the capacity is mainly due to the polarization development with cycling, which is evident in the galvanostatic profiles and the corresponding dQ/dV curves of the 1st and 200th cycles given in Figures 6e and f. While H1–M, M–H2, and H2–H3 are observed in the first cycle in a-Li:NCA-1:1, only the H1–M and M–H2 phase transition contributed to the capacity in the 200th cycle. While there is no change in the voltage at which phase transition occurs due to the active material's storage, there is a significant polarization development during the cycling.

To understand this behavior, the samples stored for one year are structurally characterized by XRD, FTIR, and Raman mapping and are given in Figure 7. The increase in the relative intensity of (104) w.r.t (003) in the XRD pattern of the 1-year-old sample compared to pristine is a clear indication of Ni^{2+} occupation in Li site in a-Li:NCA-1:1 and a-Li:NCA-1.03:1

(Figure 7a and b in comparison with Figure 1a and b). The quantification of Ni^{2+} occupancy in the Li^+ site is carried out by the Rietveld refinement, and the observed and calculated pattern and difference in the intensity between the observed and calculated patterns are given in Figures 7a and b. The fitted values of lattice constant, c/a , and Li^+ , Ni^{2+} , and R_{wp} are provided in Table 3. The low value of I_{003}/I_{104} (0.88) and high R-factor (0.56) of a-Li NCA-1.03:1 compared to that of a-Li:NCA-1:1 (1.10 and 0.4 respectively) suggests the higher percentage of Ni^{2+} in Li site in a-Li:NCA-1.03:1, in corroboration with Rietveld refinement calculation. In addition, the percentage of Li_2CO_3 in a-Li:NCA-1.03:1 is 9.6%, while no peaks corresponding to Li_2CO_3 are observed in a-Li:NCA-1:1. Though Li_2CO_3 peaks are absent, the increase in the intensity of (104) peak w.r.t to (003) in a-Li:NCA-1:1 compared to the pristine samples, suggests the possible presence of amorphous Li_2CO_3 or LiOH .

Further, Raman and FTIR analysis of the samples were carried out, which are given in Figures 7c and d. The presence of FTIR peaks at $\sim 1423 \text{ cm}^{-1}$ and 1493 cm^{-1} , corresponding to C–O symmetric and asymmetric stretching, confirms the presence of Li_2CO_3 in both samples. The intensity of Raman spectra is normalized to obtain semi-quantitative information on the concentration of Li_2CO_3 , w.r.t NCA. In the case of a-Li:NCA-1.03:1, the intensity of Li_2CO_3 peaks is higher than that of NCA, while in a-Li:NCA-1:1, it is lower. This suggests that a-Li:NCA-1.03:1 has a higher concentration of Li_2CO_3 . Since the overall quantity of Li_2CO_3 and Ni^{2+} in the Li site is higher in a-Li:NCA-1.03:1, the electrochemical performance is inferior to a-Li:NCA-1:1. From XRD, FTIR, and Raman, it can be confirmed that while a-Li:NCA-1.03:1 has both amorphous and crystalline Li_2CO_3 , while a-Li:NCA-1:1 has only amorphous Li_2CO_3 . The crystalline phase forms during the synthesis of NCA, while amorphous Li_2CO_3 forms during storage. The formation of Li_2CO_3 , even when the sample is stored in a glove box, is in accordance with the observation of.^[9,20] The stable oxidation state of Ni is 2+; hence, during storage, Ni^{3+} oxidized to Ni^{2+} along with the oxidation of lattice oxygen, according to the following equation.



When the material is exposed to the atmosphere, it reacts with H_2O and CO_2 and forms Li_2CO_3 according to the following reaction.



Table 3. Rietveld Refined structural data of aged NCA samples lattice constant, a/c and Li^+ , Ni^{2+} .

Sample	a (\AA)	c (\AA)	c/a	Li^+	Ni^{2+}	R_{wp}
a-Li:NCA-1:1	2.867	14.174	4.943	0.89	0.11	4.41
a-Li:NCA-1.03:1	2.870	14.189	4.943	0.789	0.210	4

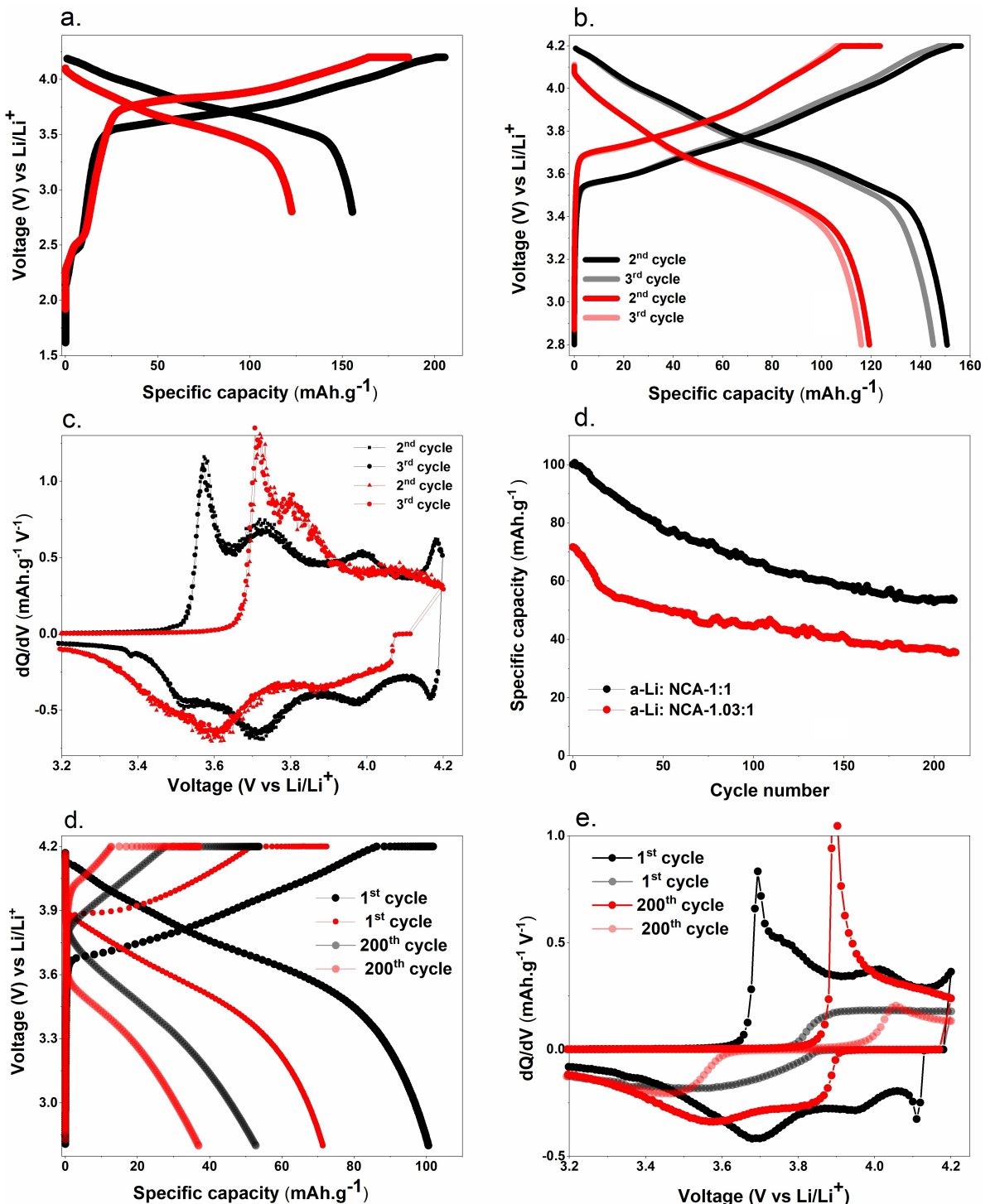
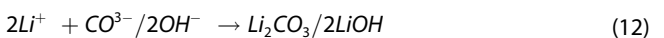


Figure 6. Galvanostatic charge-discharge of a-Li:NCA-1:1 and a-Li:NCA-1.03:1 (a) 1st cycle (b) 2nd and 3rd cycle (c) incremental capacity curves of 2nd and 3rd cycle (d) discharge specific capacity vs cycle number (e) Galvanostatic charge-discharge of 1st and 200th cycle at 1 C (f) corresponding incremental capacity curves. Symbol guide: black dots: a-Li:NCA-1:1, red dots a-Li:NCA-1.03:1



To understand the distribution of Li₂CO₃ and LiOH, Raman image scanning of the sample a-Li:NCA-1:1 and a-Li:NCA-1.03:1 was carried out. The corresponding Raman scanning

averaged 0.5 μm², and the standard deviation is given in Figure S7. Raman spectra are homogenous in a-Li:NCA-1:1. The deviation in the spectra of a-Li:NCA-1:1 is higher, as shown in Figure S7b. In the case of a-Li:NCA1:1, the spectra at different locations match close to one of the four spectra (designated as I–IV) given in Figure 8a. In the case of a-Li:NCA-

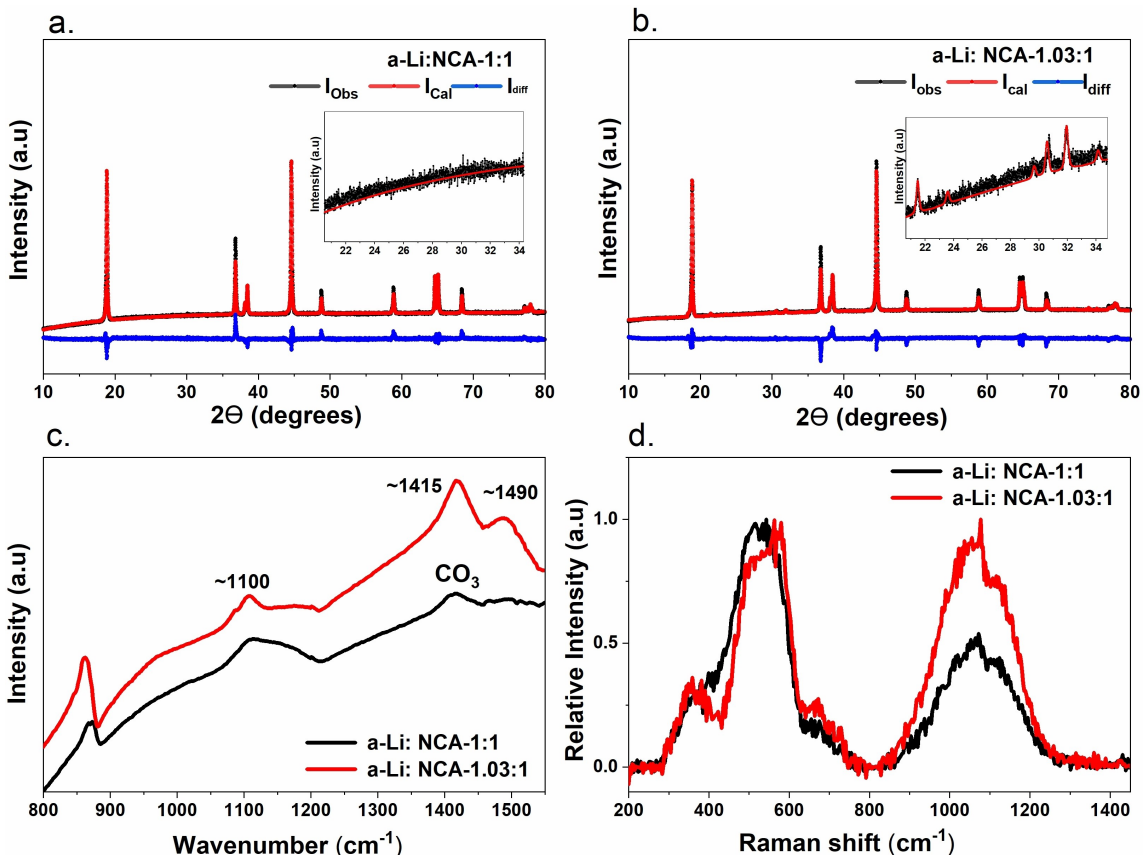


Figure 7. XRD of (a) a-Li:NCA-1:1 (b) a-Li:NCA-1.03:1 (c) FTIR and (d) Raman spectra.

1.03:1, the spectra at different locations resemble one of the three spectra shown in Figure 8b (designated as I–III). The peaks assigned to NCA are marked with *, while those assigned to LiOH/Li₂CO₃ are marked with # in the Raman spectra given in Figure 8. The peak numbers and positions change depending on the absorbed moisture in LiOH.^[21,22,10] Depending on the lithium content in NCA, the E_g and A_{1g} positions and relative peak intensities change. Two distinct peaks appear when the lithium content in NCA decreases.^[23] The peak below 400 cm⁻¹ corresponds to Li₂CO₃, while the high-intensity second peak around 520 cm⁻¹ corresponds to NCA (marked *), and the shoulder peak to the right of the NCA peak corresponds to LiOH. The peaks above 900 cm⁻¹ correspond to hydrated LiOH or Li₂CO₃. When a broad single peak appears around ~950 cm⁻¹, it is attributed to Li₂CO₃, and when multiple low-intensity peaks appear, they are attributed to hydrated LiOH.^[24,21]

The Raman spectra of the aged samples can be divided into a broad peak ranging from 250 cm⁻¹ to 750 cm⁻¹ and a couple of peaks above 925 cm⁻¹. The peak below 725 cm⁻¹ comes from NCA, Li₂CO₃, and LiOH, and the peak above 925 cm⁻¹ is from LiOH and Li₂CO₃.^[23,25,22] The Raman image mapping of a-Li:NCA-1:1 was deconvoluted into four spectra (I–IV), with the contribution from each spectrum shown as a 3D image above the corresponding spectra. Only spectrum I shows a high concentration of hydrated LiOH, while in spectra II to IV, the relative intensity corresponding to Li₂CO₃/LiOH is lower than

the intensity of the NCA peaks. Additionally, it can be observed that the contribution from spectrum I is localized to a specific region, whereas the contributions from spectra II–IV are more widespread, suggesting that the formation of Li₂CO₃/LiOH is lower in the case of a-Li:NCA-1:1. In contrast, in the case of a-Li:NCA-1:1.03, the contribution from spectra I and III is higher, where peaks corresponding to LiOH are more pronounced. Additionally, the NCA peak exhibits two distinct peaks, confirming that lithium off-stoichiometry in this sample is significant.

Li₂CO₃/LiOH (# marked) peaks, and (b) Raman spectra of a-Li:NCA-1.03:1 at three locations on the samples designated as I to III, showing the peaks corresponding to LiOH are more pronounced. CCD counts are given on a color scale near the Raman image scan. The scale inside the Raman image scanning = 5 μm.

3. Conclusions

As synthesized NiCoAl(OH)₂ precursor was mixed with Li source in two different ratios of transition metal(OH)₂ and LiOH, i.e., 1:1 (p-Li:NCA-1:1) and 1:1.03 (p-Li:NCA-1.03:1) to investigate the influence of Lithium addition on the final LiNiCoAlO₂. The Rietveld refinement analysis of X-ray diffraction signals from both the oxides confirms the presence of about 3.7% of Li₂CO₃ impurities in p-Li:NCA-1.03:1 while it was negligible in 1:1(p-

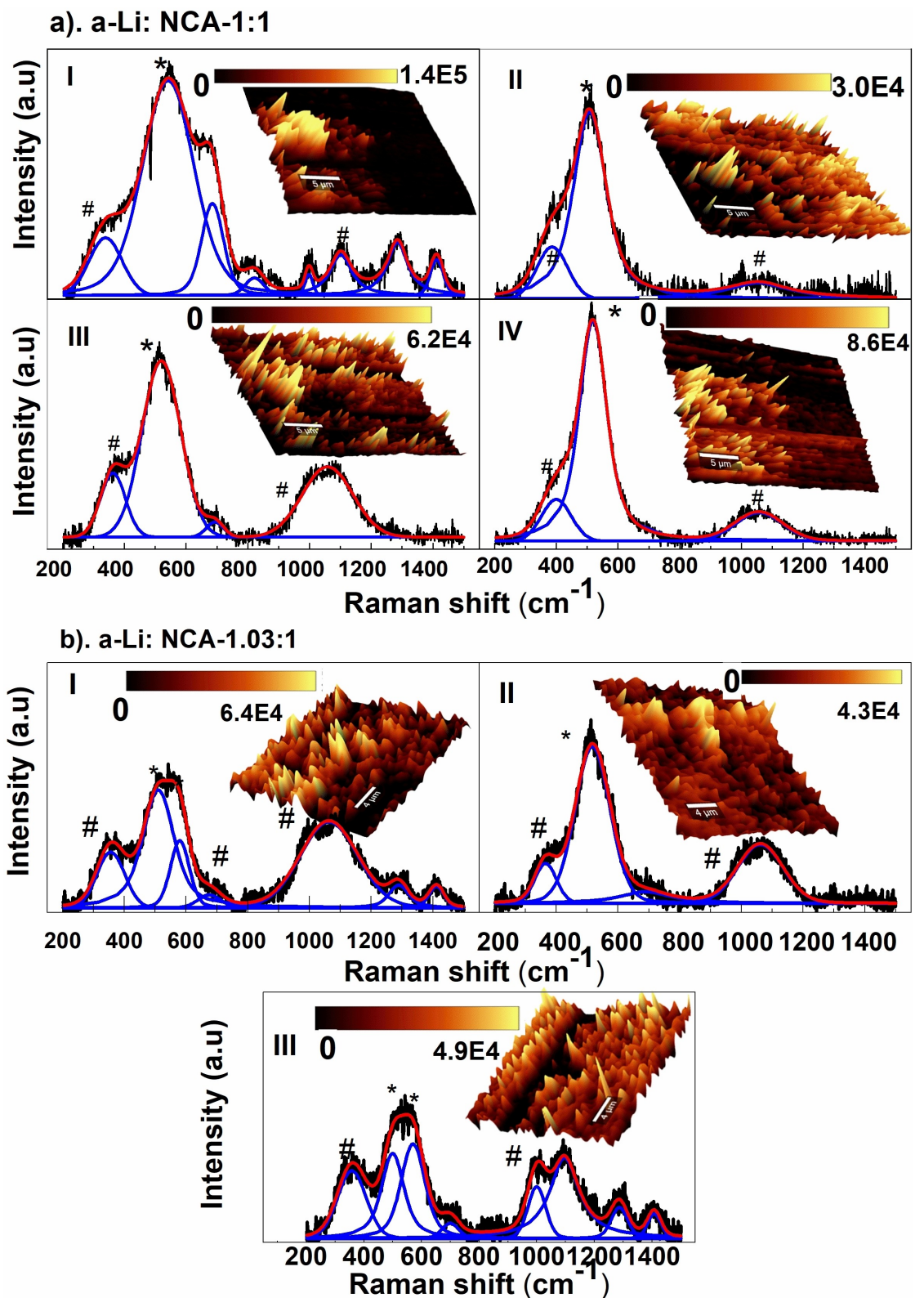


Figure 8. (a) Raman spectra mapping of aged Li:NCA-1:1 at four different locations on the

Li:NCA-1:1). Also, the peak at 1083 cm^{-1} in Raman Spectra and the two distinct broad peaks between 1400 cm^{-1} – 1500 cm^{-1} affirms the presence of Li_2CO_3 in p-Li:NCA-1.03:1. Further, the condition of Lithium residuals within the nano/micro hierarch-

ical structure of both the oxides were examined through APT analysis. A small cantilever of the sample was milled out from the center of the secondary particles using FIB technique. Mass-to-charge spectroscopy shows no traces of carbonaceous

products within the interior of both samples. Though uniform distribution of Li was observed in p-Li:NCA-1:1 throughout the sample, segregation of Li was found in p-Li:NCA-1.03:1 with the Li:TM ratio close to one at a few places and 20 at several discrete areas. The high Pearson coefficient from the frequency distribution analysis also supports the presence of segregation of Li within p-Li:NCA-1.03:1 secondary particle.

In the initial charge-discharge cycling, p-Li:NCA-1.03:1 exhibited lower discharge specific capacity, higher coulombic efficiency, and polarization compared to p-Li:NCA-1:1. In addition, the GITT profile and dq/dv vs Voltage curves at different cycles confirms the higher polarization in p-Li:NCA-1.03:1 caused by the decomposition of Li rich surface impurities leading to capacity loss and performance degradation. Both the oxide powders were stored in the argon atmosphere for almost a year to realize the shelf life after long term storage with different Li addition. From the XRD, FTIR and Raman analysis, it can be inferred that the crystalline Li_2CO_3 in p-Li:NCA-1.03:1 develops further forming amorphous Li_2CO_3 and LiOH, leading to poor electrochemical performance. Though p-Li:NCA-1:1 had negligible Li residual impurity, long-term storage results in the formation of crystalline Li_2CO_3 , resulting in lower charge-discharge capacity and cyclic stability compared to the pristine. Finally, Raman mapping confirms aggravation of Li_2CO_3 and LiOH in p-Li:NCA-1.03:1 due to non-uniform distribution and segregation of Li in the corresponding pristine sample compared to p-Li:NCA-1:1. In summary, the addition of excess Li salt to Ni rich NCA oxides paves the way for the formation of residual impurity phases on the surface and segregation of Li ions in the interior of the particle. Hence, carefully considering excess Li addition during the calcination is mandatory to maintain stoichiometry.

Author Contributions

Peddi Mahender Reddy: performing the experiments, analysis, and writing; Sasikala Natarajan: performing the experiments, plotting, analysis and writing; Nagini Macha: Performing APT and APT analysis; Raghavan Gopalan: APT methodology interpretation; Sahana B Moodakare: Conceptualization, Methodology, analysis, Investigation, Writing – Original Draft, Writing – Review & Editing, Supervision

Acknowledgements

The authors thank the Department of Science and Technology (DST) Government of India for the financial support (No. AI/1/65/ARCI/2014). The Authors acknowledge the National Facility for Atom Probe Tomography (NFAPT) at the Indian Institute of Technology Madras, Chennai, India. The authors thank the Director, ARCI, for his constant encouragement and discussion during this work. (Author 1 and Author 2 contributed equally to this work.)

Conflict of Interests

Authors do not have any conflict of interest.

Data Availability Statement

The data that support the findings of this study are available from the corresponding author upon reasonable request.

Keywords: ($\text{LiNi}_{1-x-y}\text{Co}_x\text{Al}_y\text{O}_2$ · Surface impurities · Atom probe tomography · Lithium segregation)

- [1] A. Manthiram, B. Song, W. Li, *Energy Storage Mater.* **2017**, *6*, 125–139.
- [2] Y. Lv, S. Huang, Y. Zhao, S. Roy, X. Lu, Y. Hou, J. Zhang, *Appl. Energy* **2022**, *305*, 117849.
- [3] T. Entwistle, E. Sanchez-Perez, G. J. Murray, N. Anthonisamy, S. A. Cussen, *Energy Rep.* **2022**, *8*, 67–73.
- [4] A. Chen, K. Wang, J. Li, Q. Mao, Z. Xiao, D. Zhu, G. Wang, P. Liao, J. He, Y. You, Y. Xia, *Front. Energy Res.* **2020**, *8*.
- [5] X. Huang, J. Duan, J. He, H. Shi, Y. Li, Y. Zhang, D. Wang, P. Dong, Y. Zhang, *Mater. Today Energy* **2020**, *17*, 100440.
- [6] J. Kim, Y. Hong, K. S. Ryu, M. G. Kim, J. Cho, *Electrochim. Solid-State Lett.* **2005**, *9*, A19.
- [7] K. Shizuka, C. Kiyohara, K. Shima, Y. Takeda, *J. Power Sources* **2007**, *166*, 233–238.
- [8] Y. Bi, Q. Li, R. Yi, J. Xiao, *J. Electrochim. Soc.* **2022**, *169*, 20521.
- [9] D.-H. Cho, C.-H. Jo, W. Cho, Y.-J. Kim, H. Yashiro, Y.-K. Sun, S.-T. Myung, *J. Electrochim. Soc.* **2014**, *161*, A920.
- [10] R. Jung, R. Morasch, P. Karayalali, K. Phillips, F. Maglia, C. Stinner, Y. Shao-Horn, H. A. Gasteiger, *J. Electrochim. Soc.* **2018**, *165*, A132.
- [11] C. Busà, M. Belekoukia, M. J. Loveridge, *Electrochim. Acta* **2021**, *366*, 137358.
- [12] Y. Chen, Y. Zhu, W. Zuo, X. Kuai, J. Yao, B. Zhang, Z. Sun, J. Yin, X. Wu, H. Zhang, Y. Yan, H. Huang, L. Zheng, J. Xu, W. Yin, Y. Qiu, Q. Zhang, I. Hwang, C.-J. Sun, K. Amine, G.-L. Xu, Y. Qiao, S.-G. Sun, *Angew. Chem. Int. Ed.* **2024**, *63*, e202316112.
- [13] S. Natarajan, S. B. Moodakare, P. Haridoss, R. Gopalan, *ACS Appl. Mater. Interfaces* **2020**, *12*, 34959–34970.
- [14] T.-P. Gao, K. W. Wong, K. Y. Fung, W. Zhang, K. M. Ng, *Electrochim. Acta* **2018**, *288*, 153–164.
- [15] M. Wang, A. Navrotsky, *Solid State Ionics* **2004**, *166*, 167–173.
- [16] C. Julien, M. Massot, *Phys. Chem. Chem. Phys.* **2002**, *4*, 4226–4235.
- [17] C. Julien, M. Massot, S. Rangan, M. Lemal, D. Guyomard, *J. Raman Spectrosc.* **2002**, *33*, 223–228.
- [18] A. Devaraj, M. Gu, R. Colby, P. Yan, C. M. Wang, J. M. Zheng, J. Xiao, A. Genc, J. G. Zhang, I. Belharouak, D. Wang, K. Amine, S. Thevuthasan, *Nat. Commun.* **2015**, *6*, 8014.
- [19] A. Devaraj, C. Szymanski, P. Yan, C. M. Wang, V. Murgesan, J. M. Zheng, J. Zhang, T. Tyliszczak, S. Thevuthasan, *Microsc. Microanal.* **2015**, *21*, 685–686.
- [20] W. M. Seong, Y. Kim, A. Manthiram, *Chem. Mater.* **2020**, *32*, 9479–9489.
- [21] M. H. Brooker, J. B. Bates, *J. Chem. Phys.* **1971**, *54*, 4788–4796.
- [22] V. S. Gorelik, D. Bi, Y. P. Voinov, A. I. Vodchits, B. P. Gorshunov, N. I. Yurasov, I. I. Yurasova, *J. Phys. Conf. Ser.* **2017**, *918*, 12035.
- [23] E. Flores, P. Novák, E. J. Berg, *Front. Energy Res.* **2018**, *6*, DOI 10.3389/fenrg.2018.00082.
- [24] C. Julien, *Solid State Ionics* **2000**, *136–137*, 887–896.
- [25] J. Lei, F. McLarnon, R. Kostecki, *J. Phys. Chem. B* **2005**, *109*, 952–957.

Manuscript received: December 24, 2024
Revised manuscript received: January 27, 2025
Accepted manuscript online: February 6, 2025
Version of record online: February 25, 2025